# Solution Coating of Superior Large-Area Flexible Perovskite Thin Films with Controlled Crystal Packing
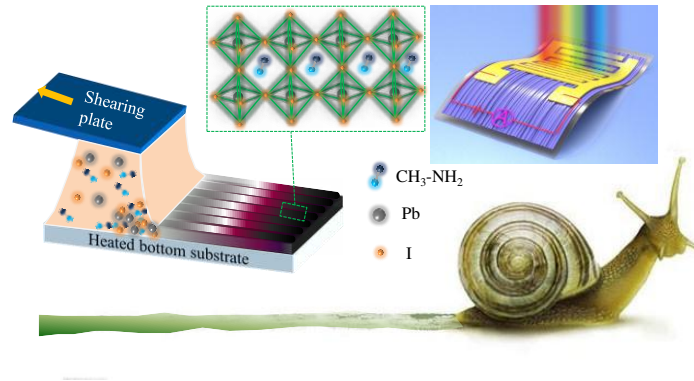
| | |
|---|---|
| Item Type | Article |
| Authors | Li, Jianbo; Liu, Yucheng; Ren, Xiaodong; Yang, Zhou; Li, Ruipeng; Su, Hang; Yang, Xiaoming; Xu, Junzhuo; Xu, Hua; Hu, Jian-Yong; Amassian, Aram; Zhao, Kui; Liu, Shengzhong (Frank) |
| Citation | Li J, Liu Y, Ren X, Yang Z, Li R, et al. (2017) Solution Coating of Superior Large-Area Flexible Perovskite Thin Films with Controlled Crystal Packing. Advanced Optical Materials: 1700102. Available: http://dx.doi.org/10.1002/adom.201700102. |
| Eprint version | Post-print |
| DOI | 10.1002/adom.201700102 |
| Publisher | Wiley |
| Journal | Advanced Optical Materials |
| Rights | This is the peer reviewed version of the following article: Solution Coating of Superior Large-Area Flexible Perovskite Thin Films with Controlled Crystal Packing, which has been published in final form at http://doi.org/10.1002/adom.201700102. This article may be used for non-commercial purposes in accordance With Wiley Terms and Conditions for self-archiving. |
| Download date | 10/08/2022 03:02:52 |
| Link to Item | http://hdl.handle.net/10754/623654 |

**TOC**



Solution shearing allows controlling crystal packing of MAPbI$_3$ perovskite in large-area printed films. The near single-crystalline perovskite thin films with a high degree of macroscopic alignment and crystal orientation exhibit excellent optical and physical properties with intense anisotropic charge transport and improved optoelectronic performance.

# Solution Coating of Superior Large-Area Flexible Perovskite Thin Films with Controlled Crystal Packing

Jianbo Li,[1,§] Yucheng Liu,[1,§] Xiaodong Ren,[1] Zhou Yang,[1] Ruipeng Li,[2] Hang Su,[1] Xiaoming Yang,[1] Junzhuo Xu,[1] Hua Xu,[1] Jian-Yong Hu,[1] Aram Amassian,[3] Kui Zhao,[1,*] Shengzhong (Frank) Liu[1,*]


*[1]Key Laboratory of Applied Surface and Colloid Chemistry, National Ministry of Education; Shaanxi Key Laboratory for Advanced Energy Devices; Shaanxi Engineering Lab for Advanced Energy Technology, School of Materials Science and Engineering, Shaanxi Normal University, Xi'an 710119, China.*

*[2]Cornell High Energy Synchrotron Source, Cornell University, Ithaca, NY 14850, U.S.A.*

*[3]King Abdullah University of Science and Technology (KAUST), KAUST Solar Center (KSC), and, Physical Sciences and Engineering Division, Thuwal 23955-6900, Saudi Arabia.*

*[§]Equal contribution.*

*\*Email: Zhaok@snnu.edu.cn; Liusz@snnu.edu.cn*

keywords: solution shearing, flexible perovskite thin films, controlled crystal packing

## Abstract

Solution coating of organohalide lead perovskites offers great potential for achieving low-cost manufacturing of large-area flexible optoelectronics. However, the rapid coating speed needed for industrial-scale production poses challenges to the control of

crystal packing. Herein we report using solution shearing to confine crystal nucleation and growth in large-area printed MAPbI$_3$ thin films. We demonstrate near single-crystalline perovskite microarrays with a high degree of controlled macroscopic alignment and crystal orientation, which exhibit significant improvements in optical and optoelectronic properties comparing with their random counterparts, spherulitic and nano-grained films. In particular, we fabricated photodetectors based on the confined films showing intense anisotropy in charge transport, and the device exhibits significantly improved performance in all aspects by one more orders of magnitude relative to their random counterparts. We anticipate that perovskite films with controlled crystal packing may find applications in high-performance, large-area printed optoelectronics and solar cells.

## 1. Introduction

Organic-inorganic hybrid perovskites have emerged as one of the most promising thin-film photovoltaic and optoelectronic materials owing to their remarkable photophysical properties.[1,2] These semiconductors combine facile fabrication with excellent optoelectronic properties, such as strong broadband light absorption,[3,4] long diffusion length,[5] and low trapping densities.[6] The certified power conversion efficiency of perovskite solar cells has arrived at 22.1%.[7] Meanwhile, the newly developed photodetectors based on large size single-crystals also attained high performances.[8-16] So far, large-size single-crystals have presented much longer charge carrier diffusion lengths and significantly lower trap-state densities,[5] but one

of the key benefits of the thin-films is that it combines flexibility with the prospect of further improvements towards continuous, high throughput roll-to-roll (R-2-R) processing.

The relative poor photophysical properties of perovskite thin-films are attributed to the inhibition of charge transport by the trap states due to random macroscopic alignment and crystal orientation that are rooted from poor crystal packing. For example, polycrystalline grains, which are always observed in spin-cast films,[17-19] exhibit large number of associated grain boundaries in which traps deteriorate quantum efficiency and photocarrier lifetime.[20] To narrow down the gap in photophysical property between the thin-films and single-crystals, it has become imperative to understand and to eventually achieve optimized crystal packing. Unfortunately, obtaining controlled packing through solution coating remains challenging, partly due to fast solvent evaporation, stochastic nucleation and fluid flow instabilities.[21,22]

There have been attempts to address above challenges. For example, 1D nanowires have been developed with fewer grain boundaries, traps, and longer photocarrier lifetime than their nano-grain counterparts.[23-25] However, fabrication of uniformly coated large-area device appears to be challenging.[26] Bakr et al. developed a thermal-gradient-assisted directional crystallization to produce fully covered periodic microarrays with high crystal orientation and anisotropic charge transport properties.[27] However the thermal-gradient-assisted directional crystallization can be readily interrupted by airflow; and the crystal formation often takes hours to complete,

making it unfavorable for high-throughput large-scale fabrication. Other approaches such as micro-gravure printing, slip-coating and blade-coating were also reported to fabricate macroscopic aligned crystals,[16,26,28] however there were no information revealed on crystal packing even though its influence is so critical on photophysical and charge transport properties.

Herein, we report using solution shearing to confine crystallization of MAPbI$_3$ in large-area printed thin films. Well controlled macroscopic alignment and crystal orientation are achieved as confirmed by optical microscopy (OM), scanning electronic microscopy (SEM), transmission electron microscopy (TEM), X-ray diffraction (XRD) and grazing incidence wide angle X-ray scattering (GIWAXS). The films with controlled crystal packing exhibit superior optical properties comparing with their random counterparts as confirmed by UV-Visible absorption, steady-state photoluminescence (PL) and time-resolved photoluminescence (TRPL). We further explored the role played by the macroscopic alignment and crystal orientation in influencing anisotropic charge transport property and optoelectronic behavior. Finally the flexibility and high stability of the photodetector based on the confined films in ambient air were confirmed.

## 2. Results and Discussion

### 2.1 Microstructure

**Figure 1a** illustrates confined crystallization process using solution shearing method. A small volume of PbI$_2$:MAI (1:1 molar ratio) solution in DMF was discharged near the gap of the shearing plate and the substrate. During the solution

shearing process, a shearing plate dragged the solution across a heated substrate at a constant velocity. The bulk of the solution was kept between the plate and the substrate, with only the evaporation front exposed. The evaporation of the solvent at the contact line (air/liquid/solid interface) causes edgeward convective flow and transport of both solvent and solute towards the contact line, resulting in confined crystallization of perovskite on the heated substrate. Certain conditions during the solution shearing process are necessary for confining crystallization that vary in substrate temperature and pulling velocity. We found an optimum condition at pulling velocity 0.2 mm s$^{-1}$ and substrate temperature 100 °C. We observed the formation of well-oriented perovskite microarrays on a large-scale flexible substrate (See Supplementary Figure S1 for more details). The scanning electron microscopy (SEM) images shows highly uniform, oriented and micrometer-wide perovskite arrays with lengths of several centimeters with the long axis parallel to the shearing direction (Figure 1b). When the shearing speed was raised to 1 mm s$^{-1}$, large isolated spherulitic morphology was observed (Figure 1c). Further increasing speed to 5 mm s$^{-1}$ leads to densely-stacked spherulitic film with isotropic packed lamellae; no preferential orientation relative to the shearing direction was observed (Figure 1d) (See Supplementary Figure S2 for more details). This trend in perovskite morphology continues up to a shearing speed of 20 mm s$^{-1}$. No macroscopic alignment is attained at lower substrate temperature. Homogeneous crystallization after shearing process results in isotropically grown fibrillar films (Figure 1e). In the cases of higher speed or lower temperature, edgeward convective flow and concentration gradient between

the bulk solution and the evaporation front during solution shearing are alleviated, leading to stochastic nucleation and crystal growth.

SEM and optical microscope images (Figure 1b and Figure S1) show no pinholes or grain-boundaries along the oriented crystals, makes it ideal to fabricate planar-type devices. Considering that spin-coated perovskite films remain by far the highly used candidate to fabricate the planar-type devices,[29-31] which show randomly-packed nano-grains on substrate due to stochastic nucleation (**Figure 1f**), the stark different crystallization behavior of the confined film motivated in-depth investigation in crystal orientation below.
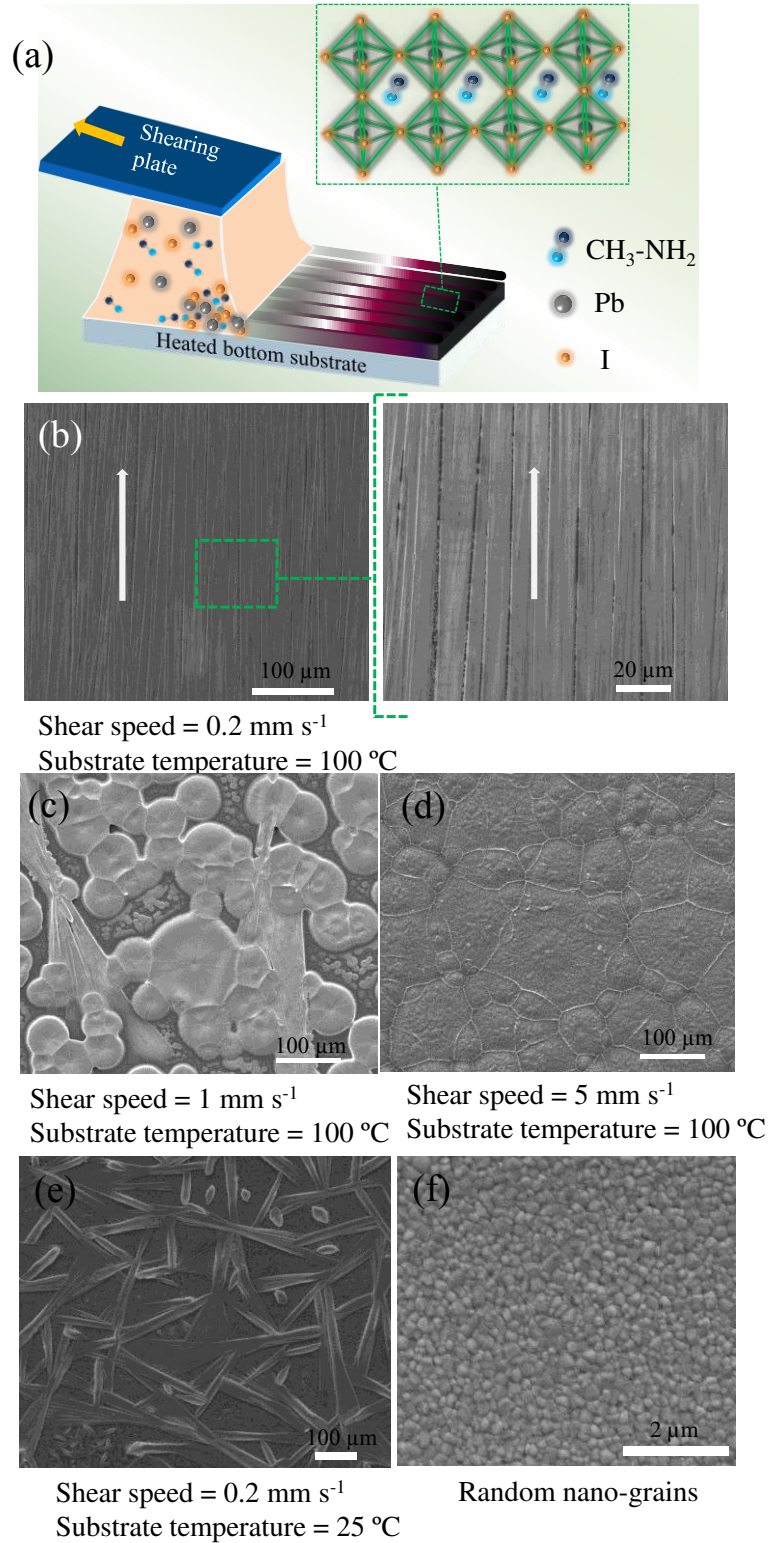
**Figure 1. Thin film growth and microstructure characterizations.** (a) Schematic illustration of confined crystallization of MAPbI$_3$ using solution shearing process. (b) Scanning electron microscopy (SEM) the magnified SEM showing the macroscopic

alignment of crystals obtained at the optimum condition. (c)-(e), SEM images of MAPbI$_3$ films formed at different shearing conditions. (f) SEM image showing the random nano-grains morphology fabricated by spin-coating method.

## 2.2 Texture characterization

Confined crystallization plays an important role in crystal packing in the thin films. X-ray diffraction (XRD), grazing incidence wide angle X-ray scattering (GIWAXS) and transmission electron microscopy (TEM) were used to characterize the coating texture.
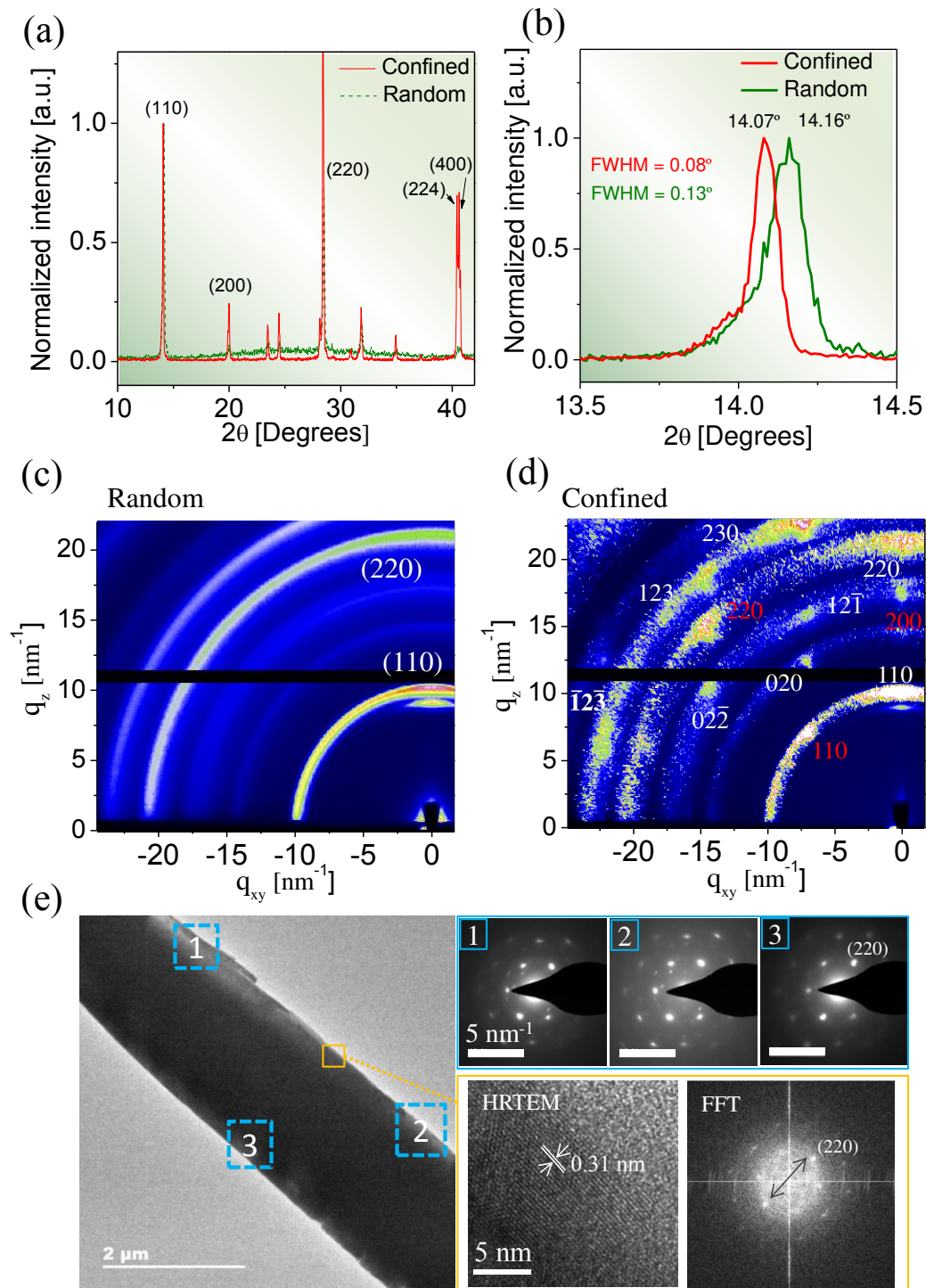
**Figure 2. Characterization of crystal structure**. (a) XRD pattern of the confined film and its random nano-grain counterparts. (b) The full width at half maximum (FWHM) of the (110) peak for both confined film and random nano-grain counterparts. (c)-(d), GIWAXS patterns showing random orientation in the random

film but well-controlled crystal orientation in the confined film, respectively. The diffraction spots shown in white belong to single-crystalline MAPbI$_3$ with the (110) plane in parallel to the substrate, while spots shown in red belong to the single-crystalline MAPbI$_3$ with the (200) plane parallel to the substrate. (e) TEM and corresponding SAED and HRTEM showing single-crystalline characteristics of the confined film.

**Figure 2a** shows XRD patterns of the confined film. We observed strong peaks at diffraction angles 2θ of 14.12° and 28.25° corresponding to the (110) and (220) planes, respectively, and peaks at 20.02° and 40.62° representing the (200) and (400) planes, respectively,[32] indicating that a tetragonal phase with main orientation along the (110) or (200) directions. Owing to the micro-spherulites shown between adjacent microarrays (Supplementary Figure S3 and Figure S4), we cannot exclude the possibility that the (224) plane seen in the confined film comes from small spherulites as the spherulitic film shows strong (224) orientation (See Supplementary Figure S5 for XRD pattern of the spherulitic film). The diffraction background for each plane was also reduced for the confined film compared to the random counterparts (spherulitic and nano-grained films) (Figure 2a and Supplementary Figure S5). The full width at half maximum (FWHM) of the (110) peak was only 0.08°, much smaller than the random nano-grained (0.13°) and the random spherulitic films (0.17°). These results confirm that confining crystallization during solution-shearing paves a way of enhancing crystallinity of thin film, which calls for in-depth crystallography

measurement using GIWAXS imaging.

GIWAXS were performed on both the confined film and its random counterparts (Figure 2b). The random perovskite films (nano-grained and spherulitic films) exhibit diffraction rings at $q=10$ $nm^{-1}$ and $q=20.2$ $nm^{-1}$ (See Supplementary Figure S6 for spherulitic films), indicating considerable randomness in the 3D orientation of the crystal domains (grains) within the polycrystalline films.[33,34] By contrast, the confined film exhibits Bragg spots along the same rings, indicating a highly-textured crystalline film in which the crystal domains are highly oriented with respect to the substrate surface. The indexed diffraction peaks show that the most of perovskite crystals pack with the (110) plane in parallel to the substrate as confirmed by the presence of the most prominent reflections. Obviously, the preferential orientation of the crystals stems from the confined nucleation and crystal growth at the contact line. Such strictly confined crystal packing has been reported in the case of cofacially stacked organic molecules, such as 6,13-bis(triisopropylsilylethynyl) pentacene (TIPS-pentacene). The confined crystallization not only induces TIPS-pen grain alignment in films, but also provides an opportunity to achieve non-equilibrium preferential orientation and molecular packing motifs.[21,22]

Small individual dots are also visible along the arc segments, likely come from the isolated small crystals between the adjacent arrays (See Figure S3). It should be pointed out that there is a (100) diffraction ring from $PbI_2$ detected at $q=9$ $nm^{-1}$ in both samples, likely from crystal decomposition caused by the high humidity (RH ≈ 55%-65%) during the GIWAXS experiment.[35] However, its intensity is relatively

weaker for the confined film than that in the random film. The slower degradation of the confined film under humidity environment was further confirmed by time-resolved XRD as shown in Figure S7.

TEM image and the corresponding selected area electron diffraction (SAED) analyses provide more details for the confined films (Figure 2e). The SAED patterns taken in three different areas of a single fiber exhibit quite similar crystal orientation and diffraction spots indexed to (220) crystalline plane of the tetragonal $MAPbI_3$ phase. The high-resolution TEM (HRTEM ) image shows crystalline lattice with spacing of 0.31 nm, consistent with the (220) plane spacing of the tetragonal $MAPbI_3$.[36] It is clear based on the above results that near single-crystalline perovskite microarrays are fabricated using the solution shearing method with a high degree of macroscopic alignment and crystal orientation.

## 2.3 Optical properties

It is known that the optical characteristics of the perovskite films is closely related to crystal packing.[37,38,39] We compared the optical absorption between two types of films. Figure 3a shows the steady-state absorption of the confined film with band-gap energy determined at 1.50 eV, slightly smaller than that of the random spherulitic film (1.55 eV)[39] and nano-grained film (1.58 eV) (Supplementary Figure S8), close to that of the large-size single-crystals and the single-crystalline wafers.[10,40] The absorption intensity of the confined film in the range of 1.5 eV-3.0 eV is also higher than that measured in its random counterparts. Likewise, the photoluminescence peak

at 1.57 eV is also red-shifted by 0.01 eV and 0.04 eV compared to the random spherulitic film and nano-grained film, respectively. The red-shifted band-edge confirms high quality of crystalline perovskite phase[5,10,41] in the confined crystals.

Time-resolved photoluminescence (TRPL) shows two-exponential decay with the fast photocarrier lifetime ($\tau_1$=3.6 ns) and slow one ($\tau_2$=104.6 ns) in the confined film (Figure 3b), assigned to surface and bulk photocarrier lifetime, respectively. The bulk photocarrier lifetime in the oriented perovskite film was 3-fold higher than that of the random counterparts, suggesting lower recombination rates. These findings confirm low trap-state density in the confined film, a critical factor for attaining high charge transport property in optoelectronics.
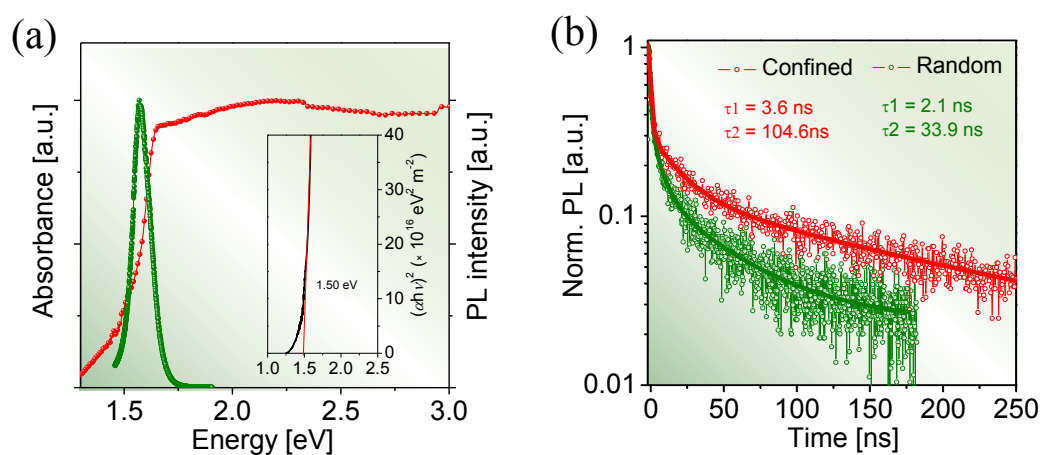


**Figure 3. Optical characterizations.** (a) Steady-state UV–Visible absorption spectrum and photoluminescence properties of the confined film. Its random counterparts were characterized and shown in Figure S8; inset showing Tauc-plot determining band-gap. (b) Time-resolved photoluminescence (TRPL) properties of the confined film and its nano-grain counterparts.

## 2.4 Optoelectronic properties

The growth of near single-crystalline perovskite microarrays with higher degree of macroscopic alignment and crystal orientation motivates development in planar flexible photodetectors. We first investigated the anisotropic charge carrier transport property in the confined film. Two different geometries of source and drain metal contacts were deposited along the shearing direction ($I_{//}$) and normal to the shearing direction ($I\perp$) as shown in Figure 4, respectively. The effective illuminated area of the device is about $2.7 \times 10^{-7}$ m$^2$. The current-voltage (*I-V*) curves of the device were measured under illumination with 560 nm light (power intensity of 22.9 mW cm$^{-2}$). We observed a significant decrease in photocurrent from $3.41 \times 10^{-6}$ in the $I_{//}$ direction to $6.68 \times 10^{-8}$ A in the $I\perp$ direction. The 50-fold decrease in photocurrent confirms that the confined film has considerable anisotropy in the charge-transport depending on the crystal orientation and grain boundaries.[27]
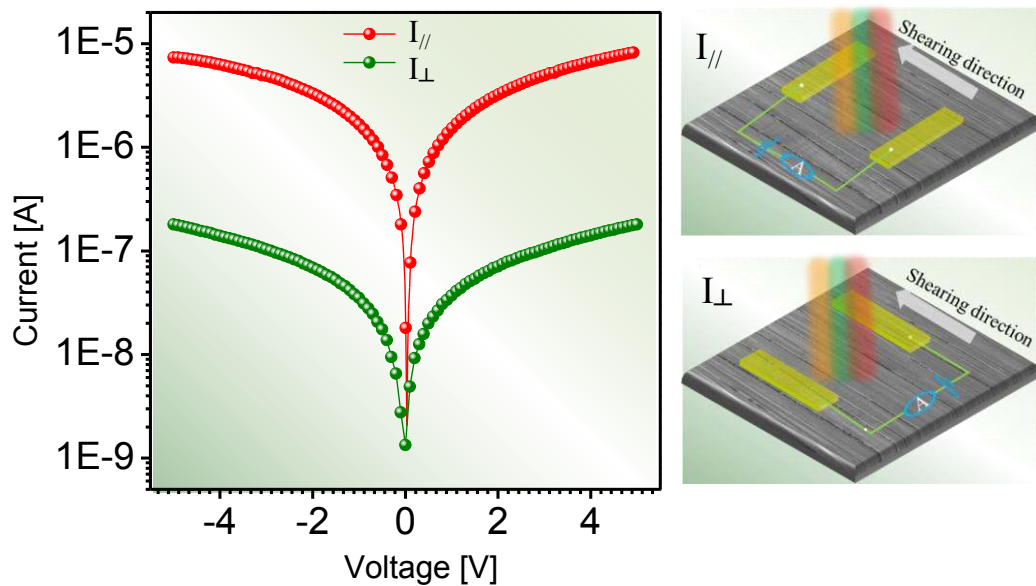


**Figure 4. Characterization of anisotropic charge transport.** The photocurrent

characteristics measured along the direction of shearing direction ($I_{//}$) and normal to shearing direction ($I\perp$), respectively.

Flexible integrated photodetectors on poly(ethylene terephthalate) (PET) with planar architecture[42] were fabricated with geometry along the shearing direction, as illustrated in Figure 5a. The device consists of 118 groups; and each group is made up of 5 pieces. The dimension of active channel between two adjacent Au pads is 1 mm in length, 40 μm in width, and ~300 nm in thickness. The effective illuminated area of the device is about $2.7 \times 10^{-7}$ m$^2$. The current-voltage (*I-V*) curves of the device were measured in the dark and under illumination with 560 nm light (power intensity of 22.9 mW cm$^{-2}$) at 2V bias.

The detector performance of the confined film was evaluated and compared with its random counterparts (nano-grains and spherulites). The current-voltage characteristic of the confined film shows a dark current of $3.34 \times 10^{-9}$ A (Supplementary Figure S9a). The current benefited from a strong contribution of photogenerated carriers under illumination, reaching to $3.41 \times 10^{-6}$ A (Figure 5b). The photocurrent decreased drastically to $0.45 \times 10^{-6}$ A for the random nano-grains (Figure 5b), and to $0.06 \times 10^{-6}$ A for the random spherulites (Supplementary Figure S9). The lowest photocurrent of the random spherulites is attributed to large amount of planar grain-boundaries between isotropic lamellae (See Supplementary Figure S2), making it less efficient for planar optoelectronic devices. In the following we only focus on quantitative analysis of detector performance for the confined crystals and random

nano-grain unless otherwise stated.

It is interesting to see that the photocurrent of the confined film is more stable comparing with the random film. A fast drop in photocurrent was observed in the random film at the first 3 sec under illumination, commonly attributed to the synergistic effect of photovoltaic effect and pyroelectric effect under illumination.[40,43,44] The pyroelectric effect was effectively alleviated in the case of the confined film. The confined perovskite also exhibits an excellent long-term photostability under continuous illumination at 560 nm (Figure S10). Moreover, the photodetector of the confined film responds much faster than that of the random film from the typical ON/OFF cycle as indicated in Figure 5c. The rise time was measured only 36 ms for the confined film and 77 ms for the random film. The decay time was also relative shorter for the confined film in contrast to the random film, 43 ms *vs* 95 ms.
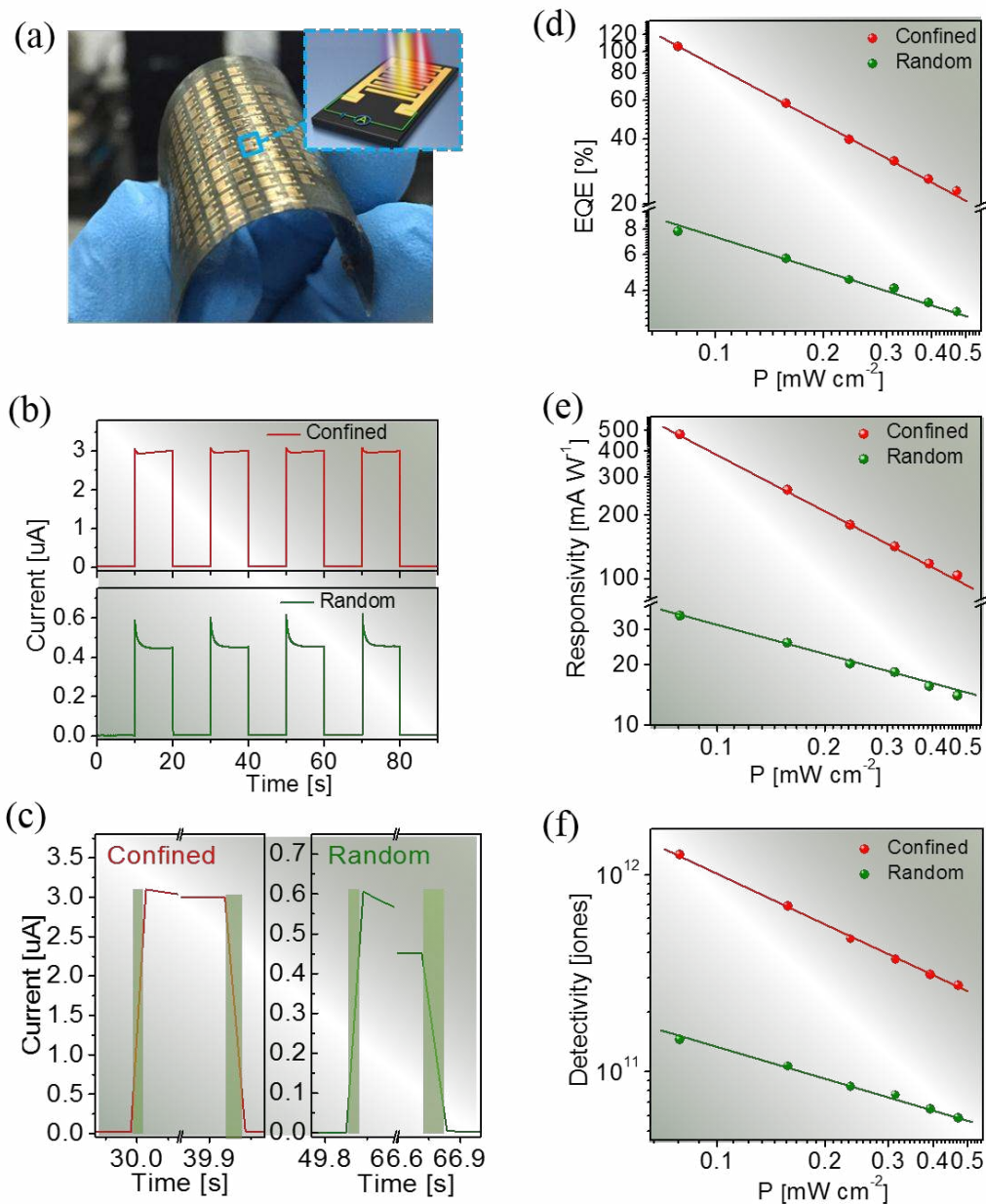
**Figure 5. Photodetector characterizations**. (a) Photo and schematic diagram showing flexible integrated photodetectors on poly(ethylene terephthalate) (PET) with planar architecture. (b) Several-cycle curves of photocurrent time response under an ON/OFF interval of 10 s illumination with 560 nm light (power intensity of 22.9 mW cm$^{-2}$) for the confined film and its random counterparts. (c) Single photocurrent response cycle with light switched ON and OFF, showing the response speed of the photodetector. <mark>The rise and decay response times were defined as the photocurrent</mark>

(d)-(f) External quantum efficiency (EQE), responsivity (R), and detectivity (D$^*$) as function of the light irradiance power density ranging from 0.08 to 0.47 mW cm$^{-2}$ at wavelength of 560 nm under a fixed 2V bias, respectively.
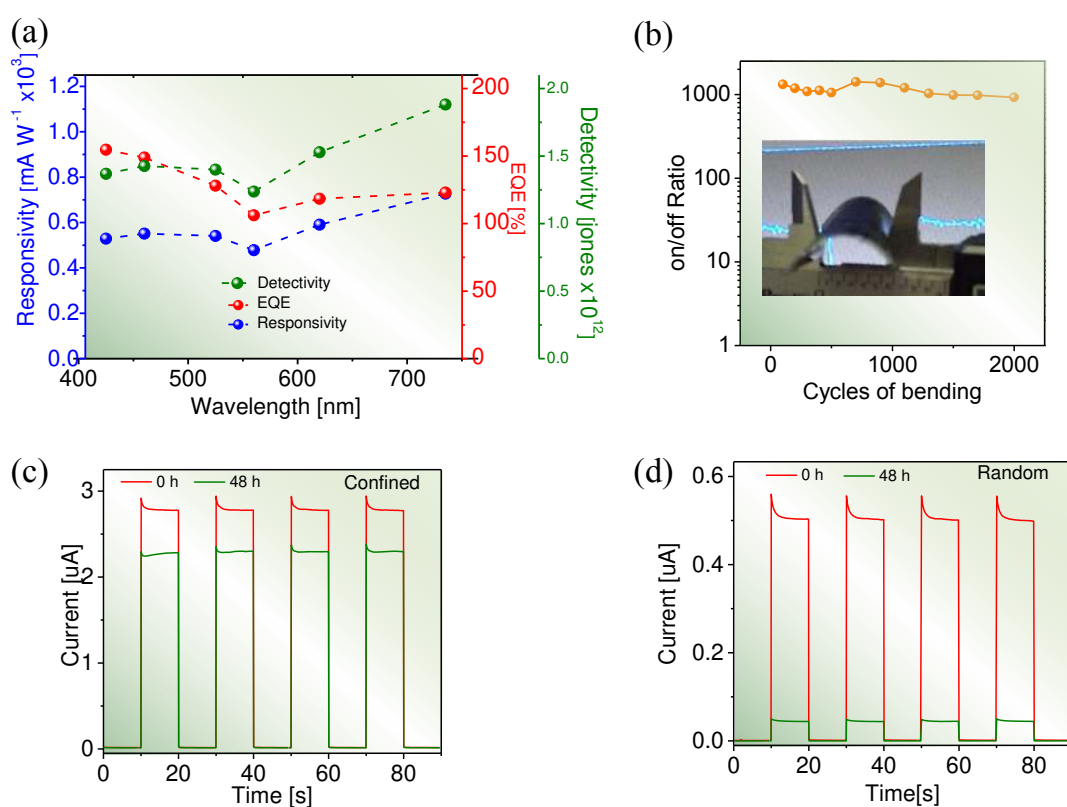


**Figure 6. Wavelength-dependent photoresponse, flexibility and stability**. (a) Spectral responsivity (R), external quantum efficiency (EQE) and detectivity (*D\**) as function of the wavelength ranging 425 nm to 730 nm at a fixed bias of 2 V for the confined film. (b) ON/OFF ratio of the flexible photodetectors made of the confined film before and after bending 2000 times. (c) and (d) Photocurrent response of the photodetectors after stored for 48 hours in ambient air (RH ≈ 50%-60%) without encapsulation for the confined film and random film, respectively.

The responsivity (*R*), external quantum efficiency (*EQE*) and detectivity (*D\**) were further determined. *R* is defined as the photocurrent generated per unit of incident power, *EQE* is defined as the number of carriers produced in the external circuit for each absorbed incident photon, *D\** is commonly used as a figure of merit reflecting the sensitivity of a photodetector. These three parameters can be expressed using the following equations:[45-49]

$$R = \frac{\Delta I}{PA} \qquad (1)$$

$$EQE = R\frac{hc}{\lambda e} \qquad (2)$$

$$D^* = \frac{R}{\sqrt{2qJ_{\text{dark}}}} \qquad (3)$$

where $\Delta I$ is the photocurrent defined as the difference between the current in the dark and under illumination, *A* the effective illuminated area, *P* the laser power density, *h* the Planck's constant, *c* the velocity of light, $\lambda$ the wavelength of incident light, *e* the elementary charge ($1.6 \times 10^{-19}$ Coulomb), *q* absolute value of electron charge ($1.6 \times 10^{-19}$ Coulomb), and $J_{dark}$ the dark current density.

Figure 5d-f shows the values of *R, EQE* and *D\** as a function of the incident light power density ranging from 0.08 to 0.47 mW cm$^{-2}$. The values of *R* and *D\** decrease at high incident light intensities following the characteristic behavior of photoconductive external quantum efficiency (*EQE*). The highest values of *R, EQE* and *D\** were estimated to be 480 mA W$^{-1}$ *vs* 35 mA W$^{-1}$, 106% *vs* 8%, and $1.26 \times 10^{12}$ Jones *vs* $1.45 \times 10^{11}$ Jones for the confined film and the random film, respectively. All relevant figures of merit are apparently enhanced significantly. We

attribute the enhanced performance of the confined film to the elimination of grain boundaries, excellent domain alignment and higher crystalline quality, enabled by confined crystallization.

The spectral photoresponse as a function of the light wavelength was further extracted for the confined film. The devices show high values in *R, EQE* and *D\** in the UV-Vis spectrum range (Figure 6a). Interestingly the photoresponse extended to 850 nm (1.46 eV) (Figure S11) with photocurrents reaching $0.22 \times 10^{-6}$ A, as indicated from the strong absorption even at the wavelength region as shown in Figure 3a.

The flexible device also shows desirable mechanical stability as the microarrays can release part of bending stress. For the test, the device was fixed in a vernier caliper bended at angle of 60° as shown in Figure 6b. The evolution of the ON/OFF ratio is essentially unchanged before and after bending for 2000 times, demonstrating excellent flexibility and a robust bending durability.

The randomly packed crystals consist of an amorphous intergranular layer in the grain-boundaries may allow quick diffusion of moisture into the perovskite films.[50,51] While large-size single crystals are much more stable in air,[10,52] we therefore evaluated the long-term stability of the flexible photodetectors based on confined crystals in ambient air with humidity level at 50-60%. As shown in Figure 6c, the photocurrent response shows only ~17% depreciation for the confined film after 2 days, while the random nano-grains degraded by ~90% (Figure 6d). The excellent stability of the confined crystal based device is attributed to the outstanding physical

properties. The high quality large-size crystals suppress the diffusion of moisture and contaminants into the inner perovskite structure, leading to more stable devices under ambient conditions.[52,53]


## 3. Conclusions

In conclusion, we have demonstrated that solution shearing allows for controlling crystal packing of MAPbI$_3$ perovskite in large-area thin films. The solution-printed films exhibit micrometers-wide, centimeters-long, highly aligned near single-crystalline microarrays, where both macroscopic alignment and crystal orientation were highly controlled. The optical properties of these confined films were distinguishable from their random counterparts in terms of absorbance, PL and photocarrier lifetime. We attribute the anisotropic charge transport property and the excellent optoelectronic performance of the confined film to the elimination of grain boundaries, excellent domain alignment and high crystalline quality. In addition, the confined films show excellent mechanical flexibility and better stability in ambient. Overall, the insights presented in this work highlight the importance of crystal packing for high-performance optoelectronics based on solution-casting films. The advantage of the solution shearing enabled us to control crystal packing of perovskites in large-area films that is not readily achievable through other fast solution-coating methods.


ASSOCIATED CONTENT

**Supporting information**

The Supporting Information is available free of charge on the ACS Publications website

AUTHOR INFORMATION

Corresponding Authors

*K.Z.: E-mail: Zhaok@snnu.edu.cn

*S.L.: E-mail: Liusz@snnu.edu.cn

Notes The authors declare no competing financial interest.

**EXPERIMENTAL SECTION**

*Solution preparation and device fabrication*: The solution preparation was conducted under inert atmosphere inside a nitrogen glove box. Perovskite precursor solution, MAI (1-Material) and $PbI_2$ (Aldrich) were dissolved (1:1 molar ratio) in

*N,N*-dimethylformamide (DMF, Aldrich) in 1 M concentration for solution-shearing. While the precursors were dissolved (1:1 molar ratio) in mixed solvents of dimethylsulfoxide (DMSO, Aldrich) and γ-butyrolactone (Aldrich, 3:7 in volume) in 1 M concentration for spin-coating. The solution was stirred overnight at 60 ºC and filtered with 0.2 μm PTFE filter before solution-casting. Glass or poly(ethylene terephthalate) (PET) substrates were cleaned through sequential sonication in ethanol, acetone and isopropanol for 15 min each and then dried with a $N_2$ blow gun. Substrate cleaning was completed through exposure to oxygen plasma for 5 min. The spin-coating was conducted under inert atmosphere inside a nitrogen glove box. The perovskite solution was coated onto the glass or flexible substrates by a consecutive two-step spin-coating process at 1,000 and 5,000 rpm for 10 and 40 s, respectively. During the second step of spin-coating, chlorobenzene was dropped on the substrate. Substrates were annealed at 100 °C for 5 minutes. The solution-shearing was performed under ambient atmosphere with speed of 10 mm/min. The as-cast films were annealed at 100 ºC for 8 minutes followed by evaporation of 100 nm gold electrode.

*Optical metrology:* UV-Visible absorption spectra were acquired on a Cary 5000 (Varian) instrument. Steady-state Photoluminescence (PL) (excitation at 532 nm) and time-resolved photoluminescence (TRPL) (excitation at 405 nm and emission at 760 nm) were measured with Edinburgh Instruments Ltd (FLS980). Optical microscopy was performed on an OLYMPUS BX51instrument.

*Electron microscopy:* Scanning electron microscopy (SEM) imaging was conducted on a field emission scanning electron microscopy (FE-SEM; SU-8020, Hitachi) at an acceleration voltage of 8 kV. Transmission electron microscopy (TEM) imaging was conducted on a FEI Tecnai G2 F20 electron microscope.

*X-ray diffraction (XRD)* measurements were carried out in a θ-2θ configuration with a scanning interval of 2θ between 10° and 60° on a Bruker D8 Discover (X-ray Source: Cu Kα; λ = 1.54 Å).

*Grazing incidence wide angle X-ray scattering (GIWAXS)* measurements were performed at D-line at the Cornell High Energy Synchrotron Source (CHESS). The wavelength of the X-rays was 1.157 Å with a bandwidth Δλ/λ of 1.5%. The scattering signal was collected by Pilatus 200K detector, with a pixel size of 172 µm by 172 µm placed at 191 mm away from the sample position. The incident angle of the X-ray beam was at 0.25 degree and the integration time was 1s.

*Optoelectronic characterizations:* The photocurrent response characteristics for the photodetectors were collected by a Keithley 2400 SourceMeter with a series of LED lasers. The high speed characteristics of the device were measured by an optical chopper and a Digital Storage Oscilloscope (Agilent DSO-X 2012A).

**REFERENCES:**

[1] A. Kojima, K. Teshima, Y. Shirai, T. Miyasaka, *J. Am. Chem. Soc.* **2009**, *131*, 6050.

[2] H.-S. Kim, C.-R. Lee, J.-H. Im, K.-B. Lee, T. Moehl, A. Marchioro, S.-J. Moon, R. Humphry-Baker, J.-H. Yum, J. E. Moser, M. Gratzel, N.-G. Park, *Sci. Rep.* **2012**, *2*, 591.

[3] S. Sun, T. Salim, N. Mathews, M. Duchamp, C. Boothroyd, G. Xing, T. C. Sum, Y. M. Lam, *Energy Environ. Sci.* **2014**, *7*, 399.

[4] J. Burschka, N. Pellet, S. J. Moon, R. Humphry-Baker, P. Gao, M. K. Nazeeruddin, M. Grätzel, *Nature* **2014**, *499*, 316.

[5] D. Shi, V. Adinolfi, R. Comin, M. Yuan, E. Alarousu, A. Buin, Y. Chen, S. Hoogland, A. Rothenberger, K. Katsiev, Y. Losovyj, X. Zhang, P. A. Dowben, O. F. Mohammed, E. H. Sargent, O. M. Bakr, *Science* **2015**, *347*, 519.

[6] A. Marchioro, J. Teuscher, D. Friedrich, M. Kunst, R. Van De Krol, T. Moehl, M. Grätzel, J. E. Moser, *Nat. Photonics* **2014**, *8*, 250.

[7] *National Renewable Energy Laboratory (NREL)*, Best Research-Cell Efficiencies Chart (as of March 2016), **2016**.

[8] M. I. Saidaminov, V. Adinolfi, R. Comin, A. L. Abdelhady, W. Peng, I. Dursun, M. Yuan, S. Hoogland, E. H. Sargent, O. M. Bakr, *Nat. Commun.* **2015**, *6*, 8724.

[9] V. Adinolfi, O. Ouellette, M. I. Saidaminov, G. Walters, A. L. Abdelhady, O. M. Bakr, E. H. Sargent, *Adv. Mater.* **2016**, DOI: 10.1002/adma.201601196.

[10] Y. Liu, Z. Yang, D. Cui, X. Ren, J. Sun, X. Liu, J. Zhang, Q. Wei, H. Fan, F. Yu, X. Zhang, C. Zhao, S. F. Liu, *Adv. Mater.* **2015**, *27*, 5176.

[11] Q. Han, S.-H. Bae, P. Sun, Y.-T. Hsieh, Y. Yang, Y. S. Rim, H. Zhao, Q. Chen, W. Shi, G. Li, Y. Yang, *Adv. Mater.* **2016**, *28*, 2253.

[12] C. Ma , Y. Shi, W. Hu, M.-H. Chiu, Z. Liu, A. Bera, F. Li, H. Wang, L.-J. Li, T. Wu, *Adv. Mater.* **2016**, *28*, 3683.

[13] Y. Lee, J. Kwon, E. Hwang, C.-H. Ra, W. J. Yoo, J.-H. Ahn, J. H. Park, J. H. Cho, *Adv. Mater.* **2015**, *27*, 41.

[14] S. Chen, C. Teng, M. Zhang, Y. Li, D. Xie, G. Shi, *Adv. Mater.* **2016**, DOI: 10.1002/adma.201600468.

[15] H. Wei, Y. Fang, P. Mulligan, W. Chuirazzi, H.-H. Fang, C. Wang, B. R. Ecker,

Y. Gao, M. A. Loi, L. Cao, J. Huang, *Nat. Photonics* **2016***,* DOI: 10.1038/NPHOTON.2016.41

[16] W. Deng, X. Zhang, L. Huang, X. Xu, L. Wang, J. Wang, Q. Shang, S.-T. Lee, J. Jie, *Adv. Mater.* **2016**, *28*, 2201.

[17] T. Salim, S. Sun, Y. Abe, A. Krishna, A. C. Grimsdale, Y. M. Lam, *J. Mater. Chem. A* **2015**, *3*, 8943-8969.

[18] Y. Shao, Y. Fang, T. Li, Q. Wang, Q. Dong, Y. Deng, Y. Yuan, H. Wei, M. Wang, A. Gruverman, J. Shield, J. Huang, *Energy Environ. Sci.* **2016**, *9*, 1752-1759.

[19] G. E. Eperon, V. M. Burlakov, P. Docampo, A. Goriely, H. J. Snaith, *Adv. Funct. Mater.* **2014***, 24*, 151-157.

[20] H.-R. Xia, J. Li, W.-T. Sun, L.-M. Peng, *Chem. Commun.,* **2014***, 50,* 13695.

[21] Y. Diao, B. C-K. Tee, G. Giri, J. Xu, D. H. Kim, H. A. Becerril, R. M. Stoltenberg, T. H. Lee, G. Xue, S. C. B. Mannsfeld, Z. Bao, *Nat. Mater.* **2013**, *12*, 665-671.

[22] G. Giri, E. Verploegen, S. C. B. Mannsfeld, S. Atahan-Evrenk, D. H. Kim, S. Y. Lee, H. A. Becerril, A. Aspuru-Guzik, M. F. Toney, Z. Bao, *Nature* **2011**, *480*, 504-509.

[23] X. Q. Liu, X. Liu, J. L. Wang, C. N. Liao, X. S. Xiao, S. S. Guo, C. Z. Jiang, Z. Y. Fan, T. Wang, X. S. Chen, W. Lu, W. D. Hu, L. Liao, *Adv. Mater.* **2014**, *26*, 7399-7404.

[24] X. Zhou, M. Y. Lu, Y. J. Lu, E. J. Jones, S. J. Gwo, S. Gradecak, *ACS Nano* **2015**, *9*, 2868-2875.

[25] P. Zhu, S. Gu, X. Shen, N. Xu, Y. Tan, S. Zhuang, Y. Deng, Z. Lu, Z. Wang, J. Zhu, *Nano Lett.* **2016**, *16*, 871-876.

[26] E. Horvath, M. Spina, Z. Szekrenyes, K. Kamaras, R. Gaal, D. Gachet, L. Forro, *Nano Lett.* **2014**, *14*, 6761-6766..

[27] N. Cho, F. Li, B. Turedi, L. Sinatra, S. P. Sarmah, M. R. Parida, M. I. Saidaminov, B. Murali, V. M. Burlakov, A. Goriely, O. F. Mohammed, T. Wu, O. M. Bakr, *Nat. Commun*. **2016**, *7*, 13407.

[28] Q. Hu, H. Wu, J. Sun, D. Yan, Y. Gao, J. Yang, *Nanoscale* **2016**, *8*, 5350-5357.

[29] A. Dualeh, N. Tétreault, T. Moehl, P. Gao, M. K. Nazeeruddin, M. Grätzel, *Adv. Funct. Mater.* **2014**, *24*, 3250-3258.

[30] N. J. Jeon, J. H. Noh, W. S. Yang, Y. C. Kim, S. Ryu, J. Seo, S. I. Seok, *Nature* **2015**, *517*, 476-480.

[31] H. Zhou, Q. Chen, G. Li, S. Luo, T. Song, H. Duan, Z. Hong, J. You, Y. Liu, Y. Yang, *Science* **2014**, *345*, 542-546.

[32] Q. Dong, Y. Yuan, Y. Shao, Y. Fang, Q. Wang, J. Huang, *Energy Environ. Sci.* **2015**, *8*, 2464-2470.

[33] S. Lilliu, J. Griffin, A. T. Barrows, M. Alsari, B. Curzadd, T. G. Dane, O. Bikondoa, J. E. Macdonald, D. G. Lidzey, *CrystEngComm.* **2016**, *18*, 5448-5455.

[34] K. Zhao, R. Munir, B. Yan, Y. Yang, T. Kim, A. Amassian, *J. Mater. Chem. A* **2015**, *3*, 20554-20559.

[35] K. W. Tan, D. T. Moore, M. Saliba, H. Sai, L. A. Estroff, T. Hanrath, H. J.

Snaith, U. Wiesner, *ACS Nano* **2014**, *8*, 4730-4739.

[36] M. Xiao, F. Huang, W. Huang, Y. Dkhissi, Y. Zhu, J. Etheridge, A. Gray-Weale, U. Bach, Y.-B. Cheng, L. Spiccia, *Angew. Chem.* **2014**, *126*, 10056-10061.

[37] Y. Liu, Y. Zhang, Z. Yang, D. Yang, X. Ren, L. Pang, S. Liu, *Adv. Mater.* **2016**, *28*, 9204-9209.

[38] D. Yang, R. Yang, J. Zhang, Z. Yang, S. Liu, C. Li, *Energy Environ. Sci.* **2015**, *8*, 3208-321.

[39] D. Yang, Z. Yang, W. Qin, Y. Zhang, S. Liu, C. Li, *J. Mater. Chem. A* **2015**, *3*, 9401-9405.

[40] Y. Liu, J. Sun, Z. Yang, D. Yang, X. Ren, H. Xu, Z. Yang, S. F. Liu, *Adv. Opti. Mater.* **2016**, *4*, 1829-1837.

[41] Y. Dang, Y. Liu, Y. Sun, D. Yuan, X. Liu, W. Lu, G. Liu, H. Xia, X. Tao, *CrystEngComm.* **2015**, *17*, 665-670.

[42] L. Colace, G. Masini, F. Galluzzi, G. Assanto, G. Capellini, L. Di Gaspare, E. Palange, F. Evangelisti, *Appl. Phys. Lett.* **2008**, *72*, 3175-3177.

[43] M. Zhong, L. Huang, H.-X. Deng, X. Wang, B. Li, Z. Wei, J. Li, *J. Mater. Chem. C* **2016**, *4*, 6492-6499.

[44] Y. Shen, X. Yan, H. Si, P. Lin, Y. Liu, Y. Sun, Y. Zhang, *ACS Appl Mater Interfaces* **2016**, *8*, 6137-6148.

[45] P. Hu, L. Wang, M. Yoon, J. Zhang, W. Feng, X. Wang, Z. Wen, J. C. Idrobo, Y. Miyamoto, D. B. Geohegan, K. Xiao, *Nano Lett.* **2013**, *13*, 1649-1654.

[46] L. Li, P. Wu, X. Fang, T. Zhai, L. Dai, M. Liao, Y. Koide, H. Wang, Y. Bando,

D. Golberg, *Adv. Mater.* **2010**, *22*, 3161-3165.

[47] X. Hu, X. D. Zhang, L. Liang, J. Bao, S. Li, W. L. Yang, Y. Xie, *Adv. Funct. Mater.* **2014**, *24*, 7373-7380.

[48] B. W. Baugher, H. O. Churchill, Y. Yang and P. Jarillo-Herrero, *Nat. Nanotechnol.,* **2014**, *9*, 262-267.

[49] X. Gong, M. Tong, Y. Xia, W. Cai, J. S. Moon, Y. Cao, G. Yu, C. L. Shieh, B. Nilsson, A. J. Heeger, *Science* **2009**, *325*, 1665-1667.

[50] W. Huang, J. S. Manser, P. V. Kamat, S. Ptasinska, *Chem. Mater.* **2016**, *28*, 303-311.

[51] Q. Wang, B. Chen, Y. Liu, Y. Deng, Y. Bai, Q. Dong, J. Huang, *Energy Environ. Sci*. **2016**, DOI: 10.1039/C6EE02941H.

[52] Z. Yang, C. C. Chueh, F. Zuo, J. H. Kim, P.-W. Liang, A. K. -Y. Jen, *Adv. Energy Mater.* **2015,** *28*, 8890-8897.

[53] J. H. Kim, S. T. Williams, N. Cho, C.-C. Chueh, A. K. -Y. Jen, *Adv. Energy Mater.* **2014,** 1401229.

# Solution Coating of Superior Large-Area Flexible Perovskite Thin Films with Controlled Crystal Packing

Jianbo Li, Yucheng Liu, Xiaodong Ren, Zhou Yang, Ruipeng Li, Hang Su, Xiaoming Yang, Junzhuo Xu, Hua Xu, Jianyong Hu, Aram Amassian, Kui Zhao, Shengzhong (Frank) Liu
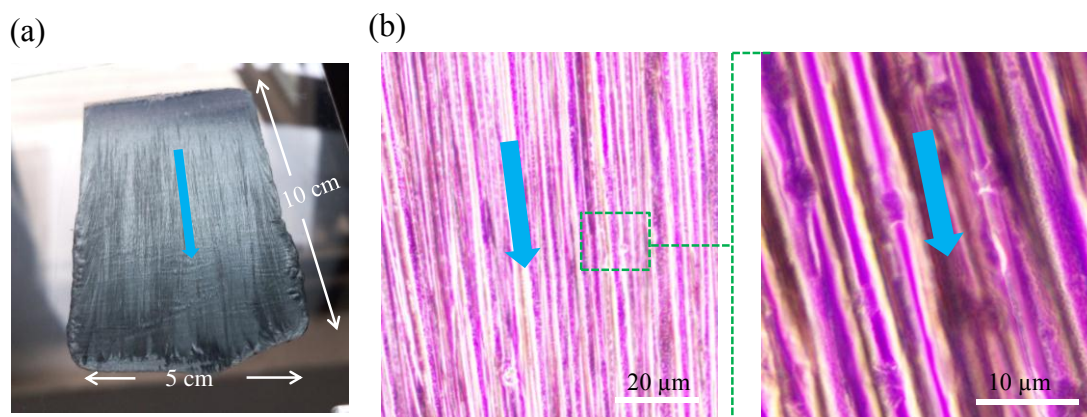


**Figure S1.** (a) Photo of large-area and flexible perovskite thin films on PET substrate fabricated using solution-shearing. (b) Dark-field optical images showing well-controlled macroscopic alignment of perovskite crystals fabricated by shear-solution.
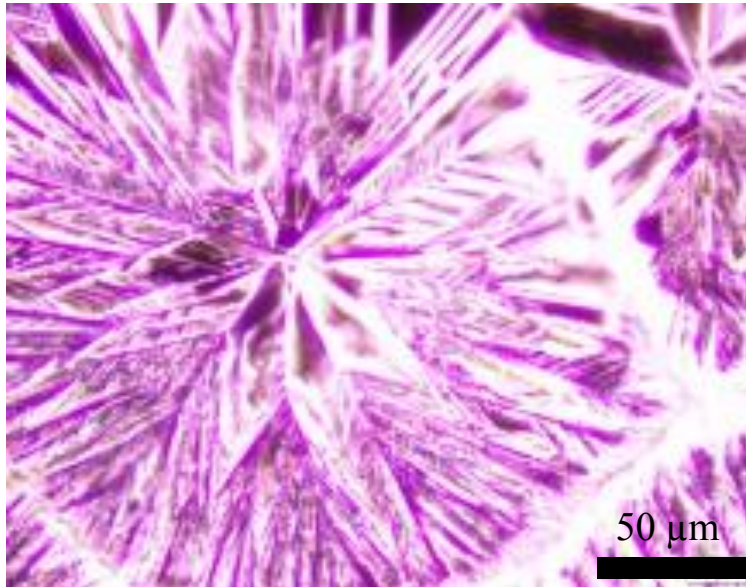
**Figure S2.** Dark-field optical image showing isotropic lamellae in the random spherulitic film.
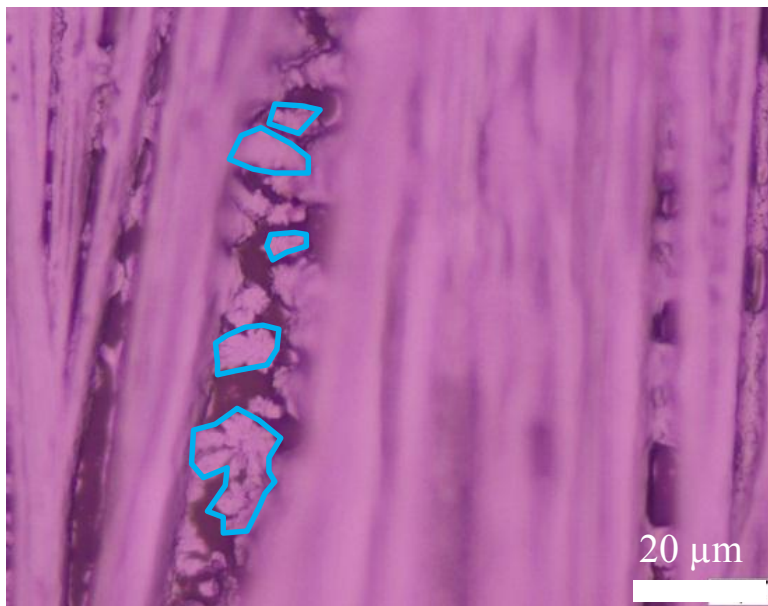


**Figure S3**. Dark-field optical image showing small spherulites and crystals between adjacent arrays.
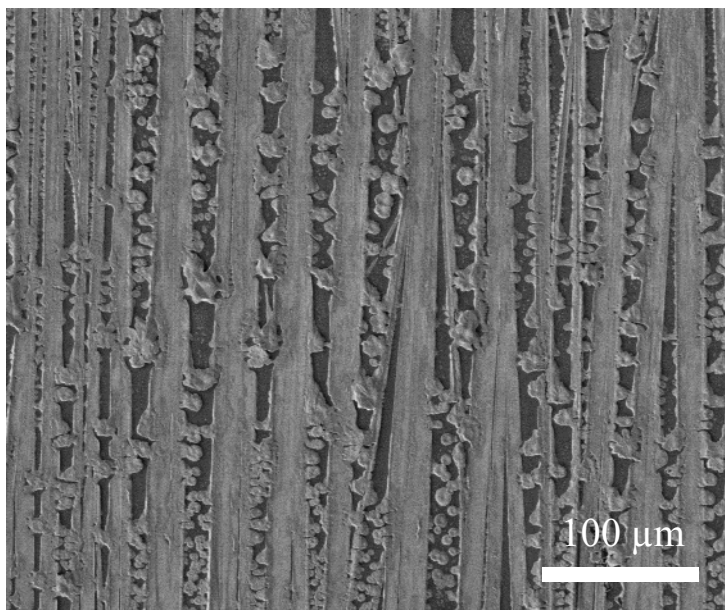
**Figure S4.** SEM image showing an increased amount of small spherulites and crystals between the adjacent arrays when decreasing solution concentration to 0.1 M.
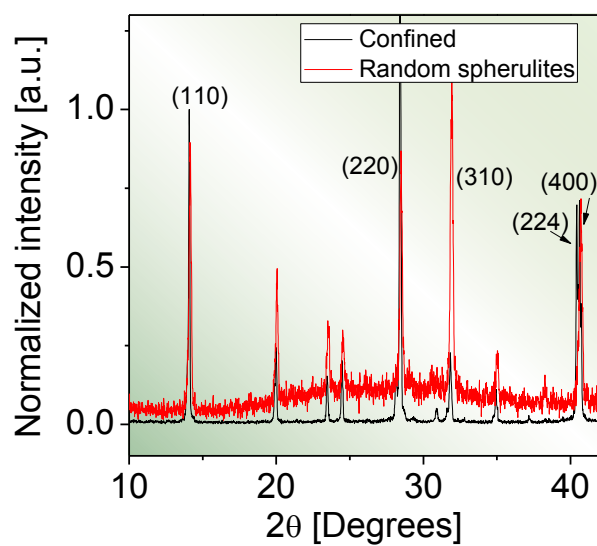


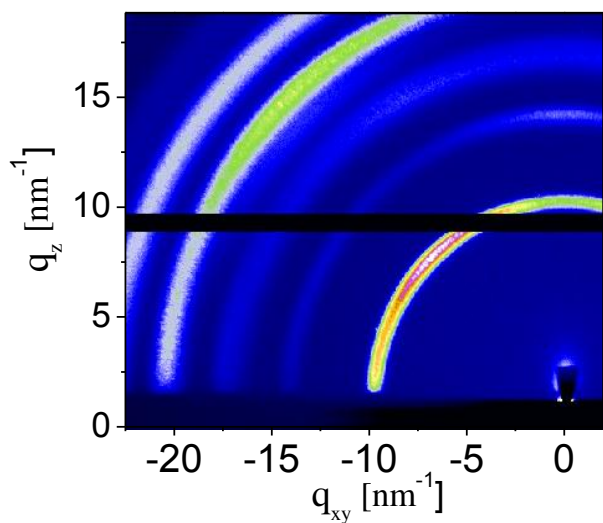**Figure S5.** XRD pattern of the confined film and its random spherulitic counterparts.

**Figure S6.** GIWAXS pattern showing 3D randomness of crystal orientation in the spherulitic film.
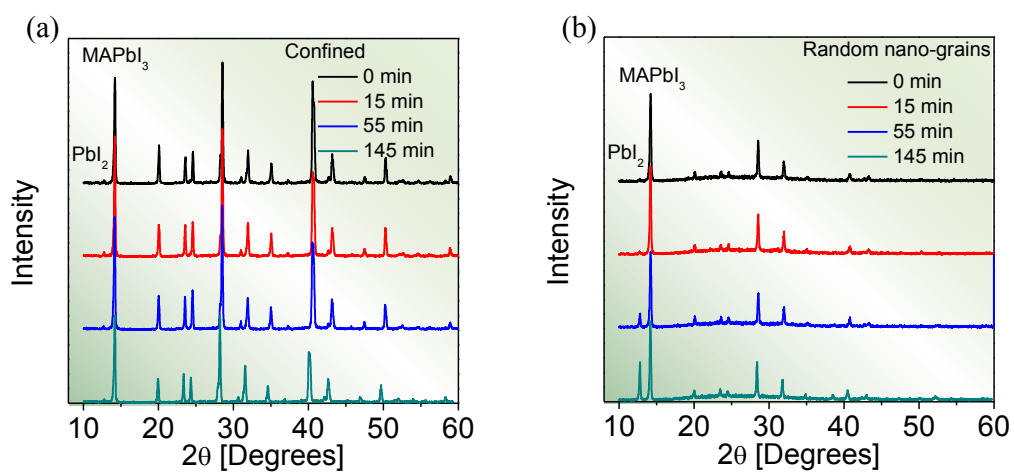


**Figure S7.**

XRD performed on the confined and random films exposed to humidity environment (75% RH) for different time showing much slower crystal decomposition of the confined film.
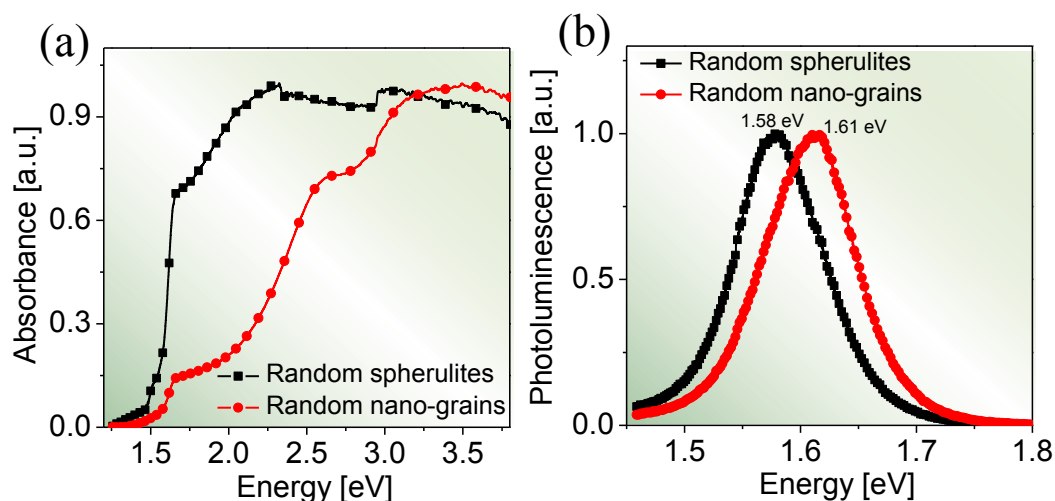
**Figure S8.** (a) Absorption and (b) photoluminescence of the random nano-grained and spherulitic films.
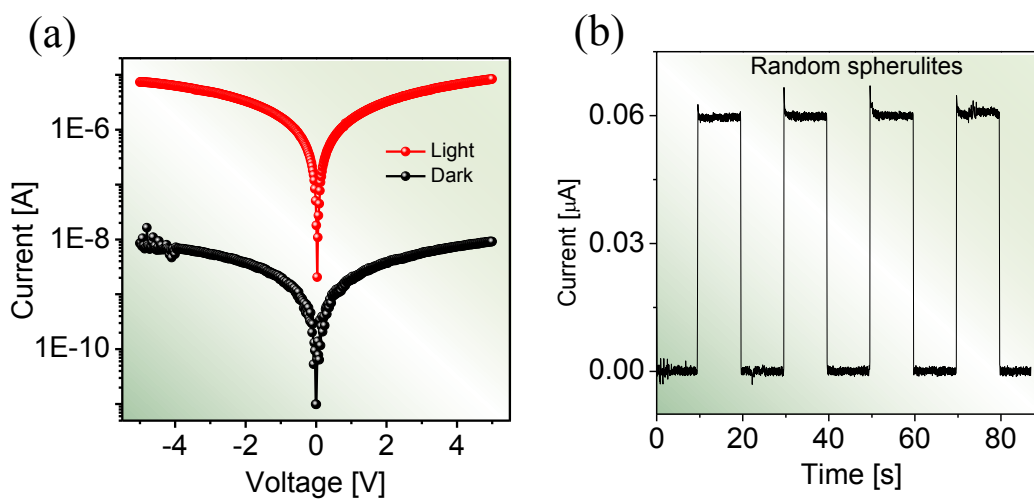


**Figure S9.** (a) *I-V* curves of the flexible device based on the confined film measured at 2 V bias in the dark and under illumination with 560 nm light (power intensity of 22.9 mW cm$^{-2}$). (b) Several-cycle curves of photocurrent time response under an ON/OFF interval of 10 s illumination with 560 nm light (power intensity of 22.9 mW cm$^{-2}$) for the random spherulitic film.
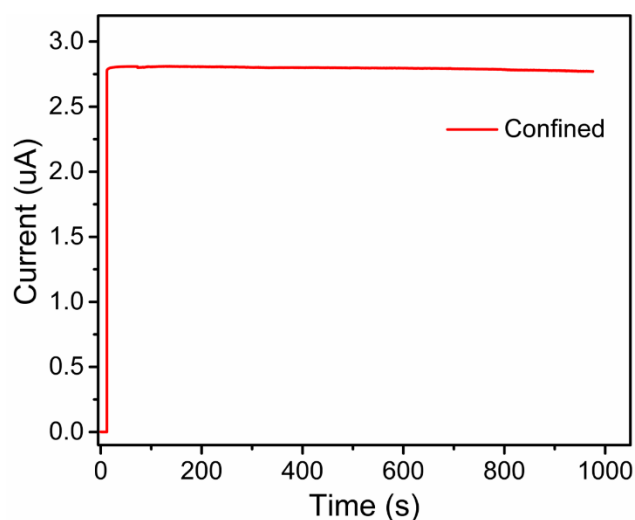
**Figure S10.** The photocurrent response of the photodetector based on the confined perovskite measured under continuous illumination at 560 nm irradiation for ~1000 seconds. The photocurrent response shows a slight depreciation by 1.5% from 2.81 μA to 2.77 μA after about ~1000 seconds illumination.
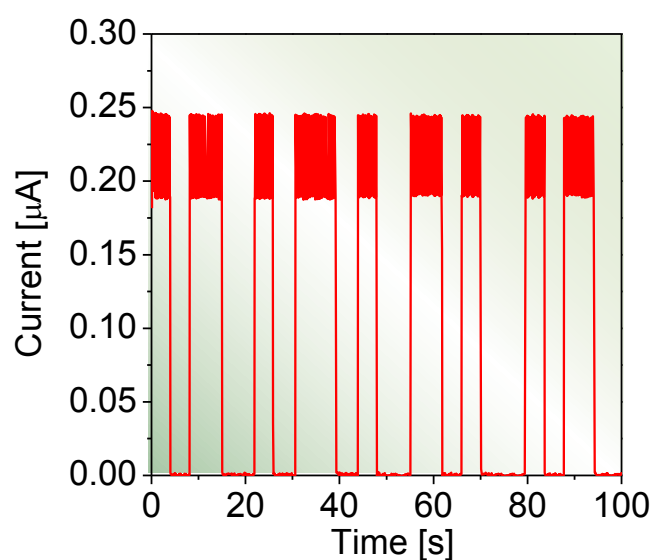


**Figure S11.** Several-cycle curves of photocurrent time response under an ON/OFF interval of 10 s illumination with 850 nm light (power intensity of 22.9 mW cm$^{-2}$).